

# DEM Construction and Calibration of Hyperspectral Image Data Using Pairs of Radiance Images

Arne M. Grumpe and Christian Wöhler  
Image Analysis Group  
Faculty of Electrical Engineering  
and Information Technology, TU Dortmund  
Otto-Hahn-Str. 4, D-44227, Dortmund, Germany  
{arne.grumpe | christian.woehler}@tu-dortmund.de

**Abstract**—In lunar remote sensing, the analysis of the spectral reflectance of iron-bearing minerals is a widely used method. For an accurate calibration, elevation information about the surface has to be known. In this paper we present a framework for the reconstruction of digital elevation maps (DEM) from hyperspectral imagery and preexisting elevation data of lower lateral resolution. The reconstruction algorithm consists of a combined photoclinometry and shape from shading scheme, which is extended towards photometric stereo using multiple images. In order to register images of the same surface region acquired under different illumination conditions, an image registration approach is derived from the DEM construction methods. Image registration is performed in the illumination-invariant surface gradient space and is therefore able to cope with images taken under different illumination conditions. Finally, the calibration of hyperspectral imagery based on the DEM is demonstrated by the analysis of extracted spectral features.

## I. INTRODUCTION

Spectral analysis of iron-bearing minerals is a common technique in lunar remote sensing (cf. [1] and references therein). In order to eliminate illumination-dependent artifacts, hyperspectral images need to be calibrated to a reference illumination geometry. A large amount of research has been done to model the reflectance behavior of planetary surfaces [2], [3]. The calibration of hyperspectral data depends on the knowledge of the position of the sun, the camera position, and the surface orientation.

Unfortunately, no pixel-synchronous digital elevation map (DEM) and image data are available in most cases, or the lateral resolution of the DEM is lower than the lateral resolution of the spectral data. Therefore, the DEM has to be registered to the images (cf. e.g. [4] as a classical example) or resampled, which yields accurate low-frequency information but may lead to interpolation artifacts. Thus the registered and resampled DEM may affect the calibration process and may lead to severe misinterpretation of the hyperspectral data.

Shape from shading (SfS) is a well-known technique which recovers depth information from images with known illumination conditions. The resulting elevation data are pixelsynchronous with the underlying image and are therefore of the same lateral resolution [5]. Many common SfS approaches assume a constant surface albedo and/or impose a smoothness constraint on the surface. It is also well known that SfS tends

to fail to recover low spatial frequency components while high-frequency details are captured correctly.

In this paper, we present an approach to combine preexisting low-resolution DEMs and hyperspectral images to reconstruct a pixel-synchronous DEM of the same lateral resolution as the spectral image. To extend this scheme towards multiple images of the same region, we develop an image registration technique based on surface gradients to register images acquired under different illumination conditions. Finally, we examine the effects of illumination on the inferred spectral characteristics of the surface material.

## II. METHODS AND DATASETS

At first, the surface reconstruction and albedo estimation algorithm is described. The algorithm can be subdivided into a photoclinometry and a SfS algorithm (although SfS and photoclinometry are widely considered to be the same, in this paper the differentiation by Horn [5] is followed). Afterwards, the utilized datasets and a method for the registration of images in the illumination-invariant surface gradient space are presented. Finally, the spectral feature maps derived from the hyperspectral data and the reconstructed DEM are discussed.

### A. Shape from Shading Algorithm

The proposed approach is an extension to the SfS scheme by Horn [5]. For the sake of readability, the explicit dependence on the lateral coordinates  $x$  and  $y$  is omitted where possible. The depth is denoted by  $z$ , the image by  $I$ , and the reflectance model by  $R$ . As proposed in [6], the pre-existing height map  $z_{\text{DEM}}$  is included into the global optimization scheme by adding a new error term  $E_{\text{DEM}}$  to Horn's intensity error  $E_I = 1/2 \iint (I - R)^2 dx dy$  and integrability error  $E_{\text{int}} = 1/2 \iint [(z_x - p)^2 + (z_y - q)^2] dx dy$ :

$$E_{\text{DEM}} = \frac{1}{2} \iint \left[ f \left( \frac{\partial z_{\text{DEM}}}{\partial x} \right) - f(p) \right]^2 + \left[ f \left( \frac{\partial z_{\text{DEM}}}{\partial y} \right) - f(q) \right]^2 dx dy \quad (1)$$

The overall error function is given by  $E = E_I + \gamma E_{\text{int}} + \delta E_{\text{DEM}}$ .  $E_{\text{DEM}}$  penalizes the deviation of the low-pass filtered surface gradients  $p$  and  $q$  from the low-pass filtered gradients of the

restricting DEM  $z_{\text{DEM}}$ . The function  $f$  is an arbitrary low-pass filter.

Following the variational approach by Horn [5] to determine  $p$  and  $q$  as well as his discrete approximation of the Laplace operator leads to the system of iterative update equations in Eq. (2), where  $n$  denotes the iteration index:

$$\begin{aligned} p^{(n+1)} &= z_x^{(n)} + \frac{1}{\gamma} \left[ I - R(z_x^{(n)}, z_y^{(n)}) \right] \frac{\partial R}{\partial p} \Big|_{z_x^{(n)}} + \\ &\frac{\delta}{\gamma} \iint \left[ f \left( \frac{\partial z_{\text{DEM}}}{\partial x} \right) - f(z_x^{(n)}) \right] \frac{\partial f(p)}{\partial p} \Big|_{z_x^{(n)}} dx dy \\ z^{(n+1)} &= \bar{z}^{(n)} - \frac{\varepsilon^2}{\kappa} \left[ p_x^{(n+1)} + q_y^{(n+1)} \right] \end{aligned} \quad (2)$$

The equation for  $q$  is obtained analogously. The variables  $\varepsilon$  and  $\kappa$  denote the lateral extension of one pixel and the number of adjacent pixels utilized for the computation of the mean value  $\bar{z}^{(n)}$ . The low-pass filter function  $f(z) = G_{\text{DEM}} \circ z$  is implemented as a correlation with a Gaussian kernel of width  $\sigma_{\text{DEM}}$ . The advantage of a linear filter operation is due to the fact that the derivatives of  $E_{\text{DEM}}$  with respect to the surface gradients are easily obtainable according to

$$\frac{\partial E_{\text{DEM}}}{\partial p} = -G_{\text{DEM}} * \left( G_{\text{DEM}} \circ \left( \frac{\partial z_{\text{DEM}}}{\partial x} - p \right) \right) \quad (3)$$

using the discrete correlation operator  $\circ$  and the discrete convolution operator  $*$ . Therefore the derivative of the error can be computed for the whole image using two consecutive linear filter operations. This still holds for the case of  $f$  being a convolution but then the order of convolution and correlation for computing the derivative has to be reversed. The approach is extended to  $N$  images by extending  $E_I$  according to

$$E_I = \frac{1}{N} \sum_{i=1}^N \frac{1}{2} (I_i - R_i)^2. \quad (4)$$

We found that the approach by Horn [5] for the simultaneous recovery of height and gradient results in an underestimation of surface slopes especially for small surface details (cf. Section III-A). Hence, to recover as much low-frequency information as possible a pyramidal approach is used, where in each pyramid step the image and the DEM are downsampled by a factor of 2 and  $\sigma_{\text{DEM}}$  is halved.

### B. Reflectance Models and Albedo Estimation

The state-of-the-art reflectance model for the lunar surface is the Hapke model [7], [8]. Two different forms of the model are used within this work. The general form of Hapke's model is given in Eq. (5). It describes the bidirectional reflectance  $R$  with respect to the incidence angle  $\vartheta_i$ , the emission angle  $\vartheta_e$ , and the phase angle  $\alpha$  according to

$$R = \frac{w}{4\pi} \frac{\mu_0}{\mu_0 + \mu} [B(\alpha)p(\alpha) + M(\mu_0, \mu)], \quad (5)$$

where  $\mu_0 = \cos \vartheta_i$  and  $\mu = \cos \vartheta_e$ . The function  $B(\alpha) = B_0 / ((1 + \tan(\alpha/2))/h)$  describes the opposition effect of strength  $B_0$  and width  $h$ . The single-scattering albedo  $w$ ,  $B_0$ ,  $h$ , and the single-scattering phase function  $p(\alpha)$  are surface

parameters. Within this study,  $p(\alpha)$  is modeled using the double-lobed Henyey-Greenstein phase function. Note that the terms due to the shadow-hiding opposition effect [7] and the coherent backscatter opposition effect [8] are combined into  $B(\alpha)$  (cf. e.g. [9]). The parameters except the albedo are taken from [9].

The difference between the applied models lies in to the multi-scattering approximation  $M(\mu_0, \mu)$ . For 3D surface reconstruction, the isotropic multiple scattering approximation (IMSA) presents an acceptable trade-off between accuracy and computation speed [7]. To ensure a maximum of accuracy for the calibration of the hyperspectral data, the more elaborate but computationally more expensive anisotropic multiple scattering approximation (AMSA) [8] is used. The analytic forms of  $M(\mu_0, \mu)$  are too long to be repeated here. They are taken from [7] and [8].

Both representations of the Hapke model share a nonlinear dependence of the surface reflectance on the single-scattering albedo  $w$ . Once the surface normal is known for each pixel,  $w$  can be computed using Newton's method. The calibrated hyperspectral data are retrieved by inserting  $w$  and a normalized illumination geometry into the model. The pixel-wise computation of  $w$  allows to deal with spatially varying albedos.

For DEM construction, the restricting DEM is used to compute an initial  $w$  map. The restricting DEM is assumed to be accurate on large scales, such that the resulting albedo  $w$  is smoothed using a Gaussian kernel of width  $\sigma_w$  to cancel out topography-related artifacts. Again,  $\sigma_w$  is halved on each pyramid step. The resulting DEM can be used as an initial surface for another reconstruction with reduced  $\sigma_w$ . This is repeated in an iterative manner for the simultaneous recovery of  $w$  and the DEM.

### C. Extended Photoclinometry Algorithm

The Sfs algorithm tends to approach a local minimum close to the initial DEM, yielding underestimated surface slopes especially on small scales. During the simultaneous recovery of height and gradient according to [5],  $p$  and  $q$  are adapted during each iteration and depend on the estimated surface  $z$ . To separate these steps,  $p$  and  $q$  are extracted from the image first. In general, photoclinometry (PHCL) is an ill-posed problem which possesses no unique solution, such that e.g. the surface gradient perpendicular to the direction of incident light is set to zero [10]. If a DEM of (possibly) lower lateral resolution is available, a solution can be obtained by solving

$$(p_{\text{PHCL}}, q_{\text{PHCL}}) = \arg \min_{p, q} (E_I + \delta E_{\text{DEM}}). \quad (6)$$

For the implementation of  $G_{\text{DEM}}$  using a Gaussian filter it can be shown that  $E_{\text{DEM}}$  is convex and possesses only one globally attractive minimum in  $p = \frac{\partial z}{\partial x}$  and  $q = \frac{\partial z}{\partial y}$ . Therefore it can be seen as an "added pull" to the restricting DEM. The minimization is carried out using the Levenberg-Marquardt algorithm as described in [11]. The initial values for the surface gradients are taken from the restricting DEM. Finally,  $z$  is recovered from the gradient field using Horn's approach [12].

The gradients  $p$  and  $q$  were found to be optimized only parallel to the illumination direction, and the resulting gradient maps are commonly non-integrable. For highly non-integrable gradient fields the surface optimization may fail to converge. The PHCL solution yields steeper slopes on small scales and is presumably a good initialization for the SFS algorithm, which then keeps the steeper slopes and produces significantly deeper small craters (see III-A). If the gradient field strongly differs from the initial DEM, the recovery of  $z$  may fail to converge. This can be overcome by using a pyramidal approach, resulting in small changes on steps upwards the pyramid because the low-frequency data are accurate. Starting on the lowest resolution level of the pyramid, a gradient field is computed and the surface is adapted. The resulting surface is scaled to the next resolution and adapted to a new gradient field.

#### D. $M^3$ and LOLA Datasets

One focus of this work is the calibration of hyperspectral data. The Moon Mineralogy Mapper ( $M^3$ ) imagery publicly available at <http://m3.jpl.nasa.gov/m3data.html> provides lunar hyperspectral data of nearly global coverage. During the Indian Chandrayaan-1 mission the  $M^3$  instrument, a hyperspectral pushbroom sensor, acquired pixel-synchronous images of about 140 m per pixel resolution in 85 spectral channels of about 12 nm width centered between 461 and 2976 nm. For each pixel the selenographic coordinates as well as light source direction and camera viewing direction are provided. Unfortunately, the star trackers of the Chandrayaan-1 spacecraft experienced a malfunction, leading to georeferencing inaccuracies for images acquired during different orbits. For DEM construction, the channels beyond 2000 nm are neglected to avoid errors due to a thermal component because the surface temperature at the equator becomes as high as 400 K. The restricting DEM is based on the gridded map derived from Lunar Orbiter Laser Altimeter (LOLA) data (<http://pds-geosciences.wustl.edu/missions/lro/lola.htm>). It is georeferenced to the same coordinate system as the  $M^3$  images and provides elevation values relative to the mean lunar radius of 1738 km. The nominal resolution of the LOLA data is about 60 m per pixel at the lunar equator.

#### E. Gradient-based Image Registration

The inaccurate georeferencing implies the need for image registration. Although image registration in principle is a solved problem, semi-automatic registration algorithms are bound to fail on images acquired under strongly different illumination conditions, as e.g. bright crater rims in one image appear dark in the other and vice versa. To overcome this problem, an illumination independent description of the image is required. In particular, this is useful for registering images acquired during different orbits of the same instrument or registering images from different spacecraft, since most instruments use similar but not strictly identical coordinate systems.

The registration of images and DEMs has been of interest in the field of remote sensing for a long time [4], [13], [14]. Horn [4] proposes to use artificial images by illuminating the DEM under conditions matching the illumination geometry of the image. Because of this possibility to present the image under different illumination conditions, the DEM itself as well as its gradients can be considered an illumination-invariant representation of the image (a related idea is mentioned in [15], [16] but regarded there as computationally too expensive).

The proposed image registration scheme uses the surface gradients instead of the DEM itself because the computation of the surface gradients using PHCL is less time consuming than the computation of the surface. Furthermore, only the  $p$  component is used as the illumination geometry provides only weak cues for  $q$ , since the  $q$  component has almost no influence on the reflectance if the illumination direction is close to east or west.

To extract possible control points (CP), the Harris corner detector [17] is applied to the images and an identical number of CP candidates is extracted from all images. The number of CP candidates  $\tilde{n}$  is set to be twice the number  $n$  of CPs desired for determining the transformation between the images. The resulting points are matched with subpixel accuracy using normalized cross-correlation. The main part of the transformation between the images usually consists of a translation. Another major part are perspective distortions while rotations show minor influence. Therefore the pairs of corresponding CPs are considered to be characterized by the length and the direction of their connecting lines. The  $(\tilde{n} - n)/2$  CP candidates with the largest deviations from each mean value are removed from the CP candidate set. Both sets may overlap, such that the process is repeated until  $n$  CP candidates remain. Due to the 3D perspective nature of the distortions, neither affine nor projective transformation are sufficient to match the images. Therefore a fourth-order polynomial is chosen to model the transformation. To incorporate user interaction, the chosen CP pairs are presented to the user before computing the transform, and the user may add or discard CP pairs.

#### F. Spectral Features

The elemental composition of the lunar surface can be determined by evaluating distinct features of the reflectance spectrum  $R_\lambda$  [1]. Within this work, the absorption wavelength ( $\lambda_{\text{abs}}$ ), full width at half maximum (FWHM), relative absorption depth ( $\delta_{\text{abs}}$ ), and integrated band depth (IBD) of the ferrous absorption trough near 1000 nm are examined. All spectral features are computed after continuum removal as described in [1]. High-Ca and low-Ca pyroxene and Mg-rich rock such as norite can be distinguished based on  $\lambda_{\text{abs}}$ . The abundance of mafic minerals as well as the optical maturity of the soil, i.e. the period of time it has been exposed to high-energy solar irradiation, are related to  $\delta_{\text{abs}}$ . Increased values of the FWHM are indicators for the presence of olivine [18], [19]. The IBD is also correlated with the abundance of mafic minerals [20]. In addition, the spectral ratio  $R_{2817}/R_{2657}$  is computed after thermal correction. It can be used to identify

the hydroxyl absorption near 3000 nm [21]. To compensate the thermal influence, the measured reflectance is modeled as a linear combination of a standard spectrum and Planck's law, and the thermal component is subtracted from the measured reflectance.

### III. RESULTS

There are no elevation data available at the examined resolution for a direct comparison with ground truth. Thus, first a method for the estimation of the 3D reconstruction accuracy as well as the corresponding results are presented. Afterwards, the accuracy of the image registration algorithm is examined and the spectral features are discussed.

#### A. Ground Truth Estimation for the DEM Construction Algorithm

Due to the fact that no ground truth data of the lateral resolution of the  $M^3$  images (about 140 m per pixel) are available, an artificial "ground truth" is generated: The DEM obtained for a region of the lunar surface is illuminated using the determined albedo map, the known illumination and viewing directions, and Hapke's IMSA model. For the resulting artificial image all parameters are thus perfectly known. The DEM construction algorithm is then applied to the artificial image, and the resulting surface and albedo are compared to the surface and albedo utilized to create the image.

Our analysis is based on a  $M^3$  image of the lunar crater Bulialdus. The restricting LOLA DEM is filtered with  $\sigma_{\text{DEM}} = 7$  pixels and the albedo is initially filtered with  $\sigma_w = 11$  pixels. The value of  $\sigma_w$  is gradually decreased to 5 pixels over several 3D reconstruction cycles. Noteworthy, the accuracy improves with each reconstruction cycle for the LOLA-initialized SfS scheme. In case of the PHCL-initialized SfS result, the accuracy decreases for  $\sigma_w < 7$  pixels, which is the point at which topography-related artifacts begin to appear in the albedo map. Therefore the DEMs reconstructed with  $\sigma_w = 7$  pixels are compared.

The resulting DEM of the SfS algorithm (cf. Section II-A) utilizing LOLA data for initialization is unsatisfying as the RMSE amounts to 50 m for the elevation and 0.005 for the albedo. In comparison, the PHCL solution (cf. Section II-C) achieves a slightly improved result with a RMSE of 45 m. If the PHCL solution is used as an initialization of the SfS algorithm, the accuracy increases drastically. For the elevation map a RMSE of 9 m is achieved, while the RMSE for the albedo map decreases to 0.003. The average ground truth albedo corresponds to 0.390. In comparison, the LOLA DEM shows several interpolation gaps and much less small-scale detail. This indicates that accuracy and convergence of the SfS algorithm depend highly on the initial solution and that the proposed extended PHCL algorithm is a useful method to create an initial DEM rich in small-scale detail from the image and the LOLA DEM.

#### B. Evaluation of Image Registration

The result of the image registration algorithm is presented in Fig. 1. Two images with strongly different illumination directions (Fig. 1(a) and 1(d)) are converted to gradient maps (Figs. 1(b) and 1(e)) using the proposed PHCL algorithm. Based on the gradients, 500 CPs are chosen using the Harris corner detector and filtered down to 250 CPs. Note that no user interaction was involved. In order to estimate the accuracy of the resulting transformation, we performed a cross-validation procedure by applying a random permutation to the full set of CPs and afterwards dividing the set into 10 subsets of equal size. While leaving one subset out, a transformation was computed utilizing the remaining nine subsets of CPs. This was repeated until each subset had been left out once. The complete procedure was repeated for 1000 random permutations of the original CP set. The average matching error over all transformations corresponds to 0.444 pixels and the standard deviation to 0.296 pixels. Subpixel accuracy can therefore be assumed at least for areas close to the chosen CPs. As shown in Figs. 1(c) and 1(d), the main part of the transformation consists of a translation to the east.

#### C. Derived Spectral Features

The density of the CPs in the northern part of the image indicates that the registration of the southern region is most likely less accurate. Therefore only the northern region of the crater is examined. The extracted spectral features are shown in Figs. 2(a)–2(l). They are divided into three sets. First the spectral features corresponding to the data shown in Fig. 1(a) are presented in Figs. 2(a)–2(d). This image has been taken under steep illumination and is supposed to have little topography-related artifacts. Figs. 2(e)–2(h) illustrate the features derived from the data shown in Fig. 1(d) acquired under oblique illumination. Figs. 2(i)–2(l) illustrate the spectral features extracted from the mean albedo used in the registration process. Note that features of pixels with relative band depths  $\delta_{\text{abs}} < 0.02$  are set to zero because for such shallow absorptions a reliable determination of the absorption wavelength, i.e. the position of the absorption minimum, and the FWHM is not possible.

All results show a region with a high value of  $\delta_{\text{abs}}$  on the northern crater rim which is due to the high FeO content as already shown in [22]. An increase of  $\lambda_{\text{abs}}$  as well as the FWHM is apparent on the crater rim, which may be due to optically immature material. The IBD is highly correlated with  $\delta_{\text{abs}}$ . Notably,  $\lambda_{\text{abs}}$  is lower in the image with oblique illumination while  $\delta_{\text{abs}}$  and FWHM are higher. This effect appears to be systematic and also occurs on the crater floor and the flat terrain outside the crater. It may be due to inaccuracies of the parameters of the reflectance model, the reflectance model itself, or effects of the sensor. However, since the radiance ratio on the floor between steep and inclined illumination was found to be less than two, effects like sensor nonlinearities are unlikely to be the source of the observed systematic differences.

In order to examine the  $R_{2817}/R_{2657}$  spectral ratio, a thermal correction is necessary. The determined temperature maps for the examined images are shown in Figs. 2(m)–2(n). The available spectral range does not allow an accurate estimation of temperatures below 250 K, such that these pixels are masked out in the images. As shown in Figs. 2(m)–2(p), the  $R_{2817}/R_{2657}$  ratio shows a strong correlation with the areas of low temperature. A similar tendency has already been found in [23]. For higher temperatures close to the detection threshold, the  $R_{2817}/R_{2657}$  ratio is anomalously large, presumably due to imperfect thermal correction. This effect is somewhat less pronounced on the western crater rim in Figs. 2(n) and 2(p).

#### IV. CONCLUSION

From the results of the ground truth estimation, it follows that the proposed DEM construction algorithm using PHCL to obtain an initial solution followed by the proposed SfS scheme based on a combination of image data and the LOLA DEM yields pixel-synchronous elevation maps with a lateral resolution comparable to that of the utilized images and an elevation RMSE of 9 m. The large difference to the LOLA-initialized DEM construction results indicates that the choice of the initial solution is critical for the reconstruction accuracy. The optimal number of reconstruction cycles and the automatic determination of the smallest possible filter kernel sizes are subject to further research.

As shown by the regarded example of the lunar crater Menelaus, the proposed image registration algorithm is able to register images acquired under strongly different illumination conditions. The reconstruction of the surface gradients eliminates the dependencies on the illumination geometry. In the case of minor translation errors and geometric distortions, the applied blockmatching and CP filtering have produced reasonable CPs and achieved subpixel accuracy without the need for user interaction. The PHCL method was able to recover gradient maps rich in small-scale detail, while the elevation accuracy is of minor importance for the blockmatching algorithm. Future work will involve a comparison between different feature detectors, correspondence measures other than normalised cross-correlation (e.g. mutual information [24]), as well as other illumination-independent representations like the surface slope or the positions of small craters.

The constructed DEM of high lateral resolution allows a generation of maps of the wavelength-dependent single-scattering albedo according to the Hapke model and thus a normalization of the  $M^3$  hyperspectral data with respect to the illumination and viewing geometry. The derived spectral features are consistent with previous data of the crater Menelaus. Small but systematic deviations were found in the spectral features derived from images acquired under different illumination conditions. The source of these effects is still unknown. The analysis of the hydroxyl absorption reveals as a general tendency an increase of the absorption depth with decreasing surface temperature.

#### REFERENCES

- [1] C. Wöhler, A. Berezhnoy, and R. Evans, "Estimation of elemental abundances of the lunar regolith using Clementine UVVIS+NIR data," *Planetary and Space Science*, vol. 59, pp. 92–110, Jan. 2011.
- [2] A. S. McEwen, "Photometric functions for photogrammetry and other applications," *Icarus*, vol. 92, no. 2, pp. 298 – 311, 1991.
- [3] B. Hapke, *Theory of reflectance and emittance spectroscopy*. Cambridge University Press, 1993.
- [4] B. K. P. Horn and B. L. Bachman, "Using synthetic images to register real images with surface models," 1978.
- [5] B. K. P. Horn, "Height and gradient from shading," MIT, AI Lab, A.I. Memo 1105A, 1989.
- [6] A. Grumpe, S. Herbolt, and C. Wöhler, "3d reconstruction of non-lambertian surfaces with non-uniform reflectance parameters by fusion of photometrically estimated surface normal data with active range scanner data," *Proc. Oldenburger 3D Tage 2011*, vol. 10, pp. 54–61, 2011.
- [7] B. Hapke, "Bidirectional reflectance spectroscopy : 4. the extinction coefficient and the opposition effect," *Icarus*, vol. 67, no. 2, pp. 264 – 280, 1986.
- [8] B. Hapke, "Bidirectional reflectance spectroscopy: 5. the coherent backscatter opposition effect and anisotropic scattering," *Icarus*, vol. 157, no. 2, pp. 523 – 534, 2002.
- [9] J. Warell, "Properties of the Hermean regolith: IV. Photometric parameters of Mercury and the Moon contrasted with Hapke modelling," *Icarus*, vol. 167, no. 2, pp. 271–286, 2004.
- [10] C. Wöhler, R. Lena, P. Lazzarotti, J. Phillips, M. Wirths, Z. Pujic, and Geologic Lunar Research (GLR) Group, "A combined spectrophotometric and morphometric study of the lunar mare dome fields near Cauchy, Arago, Hortensius, and Milichius," *Icarus*, vol. 183, pp. 237–264, 2006.
- [11] S. Marsland, *Machine Learning: An Algorithmic Introduction*. New Jersey, USA: CRC Press, 2009.
- [12] B. K. Horn, *Robot Vision*, MIT Press, 1986.
- [13] Z. Jankó and D. Chetverikov, "Registration of an uncalibrated image pair to a 3d surface model," *Pattern Recognition, International Conference on*, vol. 2, pp. 208–211, 2004.
- [14] Z. Jankó, D. Chetverikov, and A. Ekárt, "Using genetic algorithms in computer vision: registering images to 3d surface model," *Acta Cybern.*, vol. 18, pp. 193–212, February 2007.
- [15] B. K. P. Horn, "Shape from shading," B. K. P. Horn, Ed. Cambridge, MA, USA: MIT Press, 1989, ch. Obtaining shape from shading information, pp. 123–171.
- [16] B. K. P. Horn, "Understanding image intensities," *Artificial Intelligence*, vol. 11, no. 2, pp. 201–231, 1977.
- [17] C. Harris and M. Stephens, "A combined corner and edge detector," *Proceedings of The Fourth Alvey Vision Conference (1988)*, pp. 147–151, 1988.
- [18] S. Smrekar and C. M. Pieters, "Near-infrared spectroscopy of probable impact melt from three large lunar highland craters," *Icarus*, vol. 63, pp. 442–452, Sep. 1985.
- [19] T. V. V. King and W. I. Ridley, "Relation of the spectroscopic reflectance of olivine to mineral chemistry and some remote sensing implications," *Journal of Geophysical Research*, vol. 92, pp. 11 457–11 469, Oct. 1987.
- [20] D. Dhingra, C. M. Pieters, P. Isaacson, M. Staid, J. Mustard, R. Klima, L. A. Taylor, G. Kramer, J. Nettles, and M3 Team, "Spectroscopic Signature of the High Titanium Basalts at Mare Tranquillitatis from Moon Mineralogy Mapper (M3)," in *Proc. Lunar Planet. Sci. XXXI*, 2010, abstract #2494.
- [21] R. Clark, C. M. Pieters, R. O. Green, J. Boardman, B. J. Buratti, J. W. Head, P. J. Isaacson, K. E. Livo, T. B. McCord, J. W. Nettles, N. E. Petro, J. M. Sunshine, and L. A. Taylor, "Water and Hydroxyl on the Moon as Seen by the Moon Mineralogy Mapper (M3)," in *Proc. Lunar Planet. Sci. XXXI*, 2010, abstract #2302.
- [22] A. Hayashi, B. R. Hawke, D. T. Blewett, G. A. Smith, and P. G. Lucey, "Spectral Studies of the Menelaus Region of the Moon," in *Proc. Lunar Planet. Sci. XXIX*, 1998, abstract #1838.
- [23] T. B. McCord, L. A. Taylor, T. M. Orlando, C. M. Pieters, J.-P. Combe, G. Kramer, J. M. Sunshine, J. W. Head, and J. F. Mustard, "Origin of OH/Water on the Lunar Surface Detected by the Moon Mineralogy Mapper," in *Proc. Lunar Planet. Sci. XXXI*, 2010, abstract #1860.
- [24] H. Hirschmüller, "Stereo processing by semiglobal matching and mutual information," *Pattern Analysis and Machine Intelligence, IEEE Transactions on*, vol. 30, no. 2, pp. 328–341, 2008.

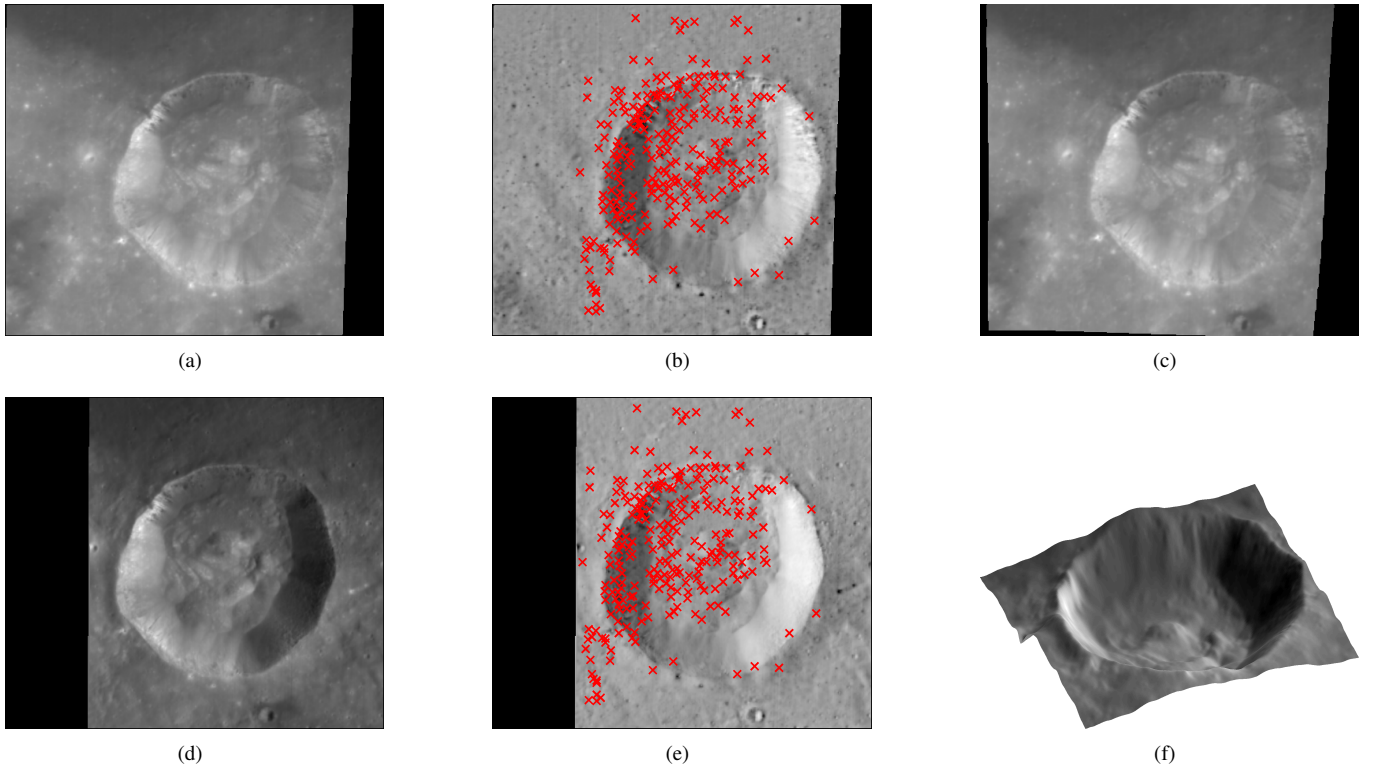


Fig. 1. Image registration results: (a)  $M^3$  spectral image at center wavelength 1978 nm with steep illumination from the south. (b) Extracted values of  $\partial z/\partial x$  and marked CPs. (c) Image after registration. (d)  $M^3$  spectral image at center wavelength 1978 nm with oblique illumination from the east. (e) Extracted values of  $\partial z/\partial x$  and marked CPs. (f) Reconstructed DEM with albedo overlay and sun position  $60^\circ$  inclined to the east. The vertical axis is 3 times exaggerated.

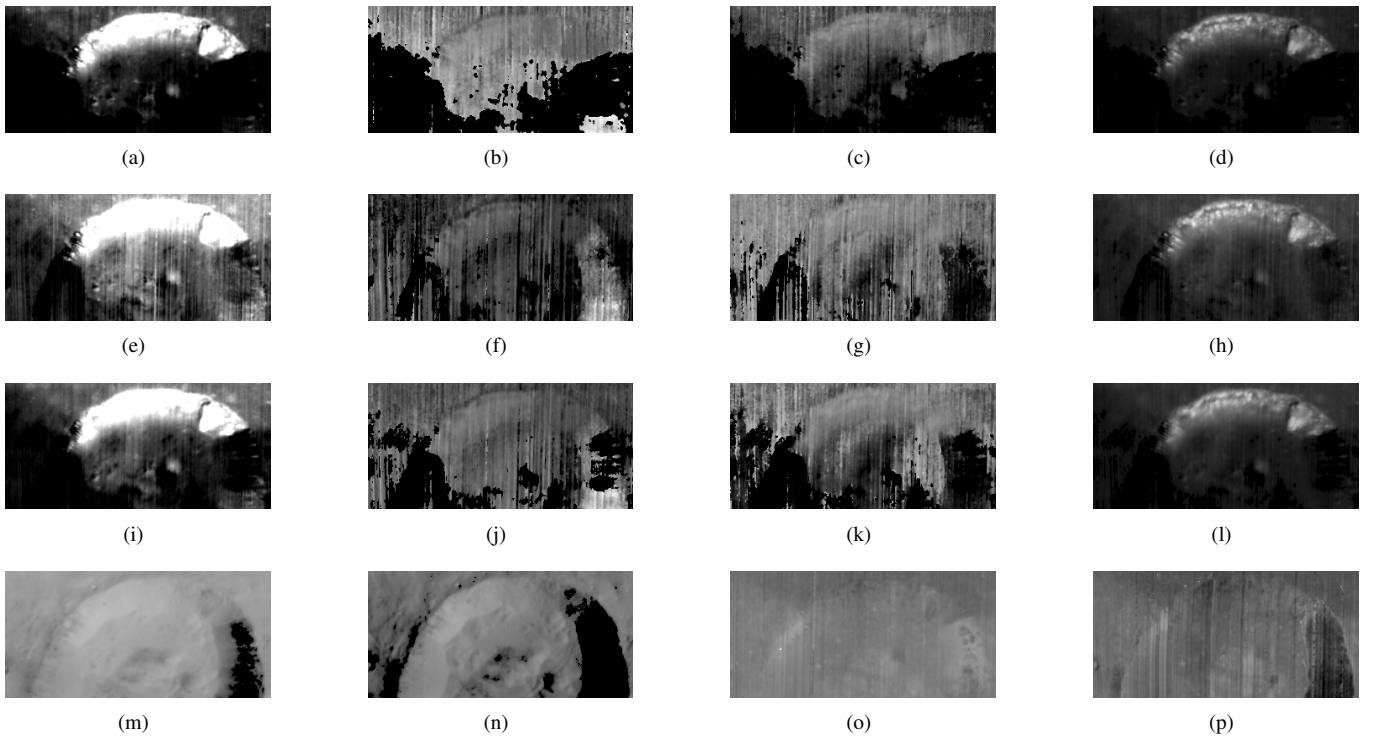


Fig. 2. Spectral features for the first set of spectral images. (a)  $\delta_{\delta_{\text{abs}}}$  (b)  $\lambda_{\delta_{\text{abs}}}$  (c) FWHM (d) IBD. Spectral feature results for the second set of spectral images: (e)  $\delta_{\delta_{\text{abs}}}$  (f)  $\lambda_{\delta_{\text{abs}}}$  (g) FWHM (h) IBD. Spectral features for combined albedo: (i)  $\delta_{\delta_{\text{abs}}}$  (j)  $\lambda_{\delta_{\text{abs}}}$  (k) FWHM (l) IBD. (m) Temperature map of the first image. (n) Temperature map of the second image. (o)  $R_{2817}/R_{2657}$  ratio of the first image. (p)  $R_{2817}/R_{2657}$  ratio of the second image. Greyscale ranges:  $\delta_{\delta_{\text{abs}}}$ : 0.02–0.1;  $\lambda_{\delta_{\text{abs}}}$ : 900 nm–1050 nm; FWHM: 150 nm–350 nm; IBD: 0–65; Temperature: 250–450 K;  $R_{2817}/R_{2657}$ : 0.9–1.1